Sharon, J., & Givol, D. (1976) *Biochemistry 15*, 1591–1594.
Skerra, A., & Plückthun, A. (1988) *Science 240*, 1038–1041.
States, D. J., Haberkorn, R. A., & Ruben, D. J. (1982) *J. Magn. Reson. 48*, 286–292.
Tsunenaga, M., Goto, Y., Kawata, Y., & Hamaguchi, K. (1987) *Biochemistry 26*, 6044–6051.
Ward, E. S., Gussow, D., Griffiths, A. D., Jones, P. T., & Winter, G. (1989) *Nature 341*, 544–546.
Wright, P. E., Dyson, H. J., Lerner, R. A., Riechmann, L., & Tsang, P. (1990) *Biochem. Pharmacol. 40*, 83–88.
Wüthrich, K. (1986) in *NMR of Proteins and Nucleic Acids*, Wiley, New York.

Oligomeric Domain Structure of Human Complement Factor H by X-ray and Neutron Solution Scattering†

Stephen J. Perkins,*,‡ Adam S. Nealis,‡ and Robert B. Sim§

Department of Biochemistry and Chemistry, Royal Free Hospital School of Medicine, Rowland Hill Street, London NW3 2PF, U.K., and MRC Immunochemistry Unit, Department of Biochemistry, University of Oxford, South Parks Road, Oxford OX1 3QU, U.K.

Received August 27, 1990; Revised Manuscript Received November 27, 1990

ABSTRACT: Factor H is a regulatory component of the complement system. It has a monomer M_r of 150000. Primary structure analysis shows that the polypeptide is divided into 20 homologous regions, each 60 amino acid residues long. These are independently folding domains and are termed "short consensus repeats" (SCRs) or "complement control protein" (CCP) repeats. High-flux synchrotron X-ray and neutron scattering studies were performed in order to define its solution structure in conditions close to physiological. The M_r of factor H was determined as 250000–320000 to show that factor H is dimeric. This structure is maintained at concentrations between 1 and 11 mg/mL in the pH range 5–9. Zn^{2+} ions are an inhibitor of C3b cleavage by factor I, a reaction in which factor H acts as a cofactor. Additions of Zn^{2+} to factor H caused it to form oligomers containing 4–10 monomers. The radius of gyration R_G of native factor H by X-rays or by neutrons in 0% or 100% ^2H_2O buffers is not measurable but is greater than 12.5 nm. Two cross-sectional radii of gyration $R_{XS\text{-}1}$ and $R_{XS\text{-}2}$ were determined as 3.0–3.1 and 1.8 nm, respectively. Analyses of the cross-sectional intensities show that factor H is composed of two distinct subunits. The $R_{XS\text{-}1}$ corresponds to the cross-sectional properties of both subunits and exhibits an unusual radiation dependence on the X-ray flux. Since $R_{XS\text{-}2}$ is close to the corresponding R_{XS} of C4b binding protein (91% of which is formed from SCR/CCP domains), it is inferred that the SCR/CCP domains of factor H and C4b binding protein have similar solution structures. The use of hydrodynamic spheres to reproduce literature sedimentation coefficients of 5.5–5.6 S showed that these were compatible with a V-shaped arrangement of two rods (36 spheres each, length 87 ± 5 nm) joined at an angle of 5°. The use of a similar arrangement of 244 spheres arranged in two rods (length 77 nm) to fit the experimental X-ray and neutron scattering curves showed that the two rods are joined at an angle of 5°. This model corresponds to an actual R_G of 21–23 nm. The separation between each SCR/CCP in factor H is close to 4 nm. In the solution structure of factor H, the SCR/CCP domains are in a highly extended conformation.

In the alternative pathway of the complement cascade of immune defense, factor H (0.2–0.6 mg/mL in plasma) is a regulatory component that serves as the cofactor for the factor I mediated cleavage of component C3b into iC3b. Factor H also accelerates the decay of the C3 convertases of the alternative pathway and inhibits their formation. Both roles are mediated by the noncovalent binding of factor H to free or surface-bound C3b or to C3b in its binary complex with factor Bb and ternary complex with Bb and properdin. The interaction between factor H and C3b therefore plays a central role in complement activation and control. Analogous roles in the complement cascade are performed on C3b or its homologue C4b by the membrane-bound complement proteins CR1 (complement receptor type 1), decay accelerating factor, and membrane cofactor protein, and by the soluble protein C4BP (C4b binding protein) [see Reid et al. (1986), Sim et al. (1987), and Reid and Day (1989) for recent reviews].

The most frequently occurring structural domain found in complement components is termed the short consensus repeat and occasionally as the short complement repeat (SCR); it is also known as the complement control protein (CCP) repeat (Sim & Perkins, 1989). Sequences for mouse and human factor H show that both are entirely formed from 20 SCR/CCPs (Kristensen & Tack, 1986; Ripoche et al., 1988). The C3b binding site of factor H and the cofactor activity for factor I both reside within the N-terminal (M_r 38000) tryptic fragment of factor H (Alsenz et al., 1985), which arises from a single proteolytic cleavage within the sixth SCR/CCP (Ripoche et al., 1988). A truncated form of factor H containing only the first seven SCR/CCPs also has cofactor activity for factor I (Ripoche et al., 1988; Misasi et al., 1989). The N-terminal five SCR/CCPs in factor H thus constitute a functionally active region.

Knowledge of the physical structures of both C3b and factor H is required to understand their roles. For C3, evidence from sedimentation data, electron microscopy, and neutron and

† We thank the Wellcome Trust, the Medical Research Council, and the Science and Engineering Research Council for support.
* Author to whom correspondence should be addressed.
‡ Royal Free Hospital School of Medicine.
§ University of Oxford.

0006-2960/91/0430-2847$02.50/0

synchrotron X-ray solution scattering studies suggests that C3 has a two-domain structure constructed from the C3c fragment (of size 2 nm × 8 nm × 18 nm) and the C3dg fragment (2 nm × 4 nm × 9 nm). This structure appears to become more compact on the removal of the small C3a anaphylatoxin when activated to C3b (Perkins & Sim, 1986; Perkins et al., 1990a). The structure of factor H is less well-known. Evidence from Fourier transform infrared spectroscopy of factor H and sequence analyses show that each SCR/CCP is formed as a β-sheet sandwich (Perkins et al., 1988). SCR/CCPs appear to form highly elongated arrangements, as first visualized by electron microscopy, solution scattering, and hydrodynamic studies for C4BP (Dahlbäck et al., 1983; Perkins et al., 1986). First evidence that factor H was also elongated is provided by reports of a high frictional ratio of 2.1 and electron microscopy studies (Whaley & Ruddy, 1976; Sim & DiScipio, 1982; Smith et al., 1983).

In application to factor H, high-flux X-ray and neutron solution scattering studies (Perkins, 1988a,b) will yield its domain structure under physiological conditions in more detail than previously, and also its molecular weight, i.e., the degree of oligomerization. The joint use of both radiations is complementary. The advantages of synchrotron X-ray scattering are as follows: (a) high positive solute–solvent contrasts are used, which facilitate modeling of the scattering curves; (b) the primary beam is highly monochromatic and collimated, which minimizes systematic errors in data collection; (c) the hydrated structure is observed. Those for neutron scattering are as follows: (a) the ability to calculate absolute molecular weights as a control; (b) the availability of a wide range of contrasts to check the data; (c) observation of the "dry" unhydrated structure, which complements the X-ray measurements; (d) absence of radiation damage effects. In application to factor H, the scattering curve analyses are constrained by the knowledge that this has a known composition with 20 SCR/CCPs. The molecular modeling of the scattering data will therefore provide information on the arrangement of the 20 SCR/CCPs in solution. Calculations of sedimentation coefficients based on hydrodynamic spheres provide a critical control of the modeling. The resulting model for factor H can be compared with those developed for C3 and C3b (Perkins & Sim, 1986; Perkins et al., 1990a).

Materials and Methods

Purification of Factor H. Factor H was isolated from outdated human plasma (kindly donated by the Regional Blood Transfusion Service, Oxford) by the method of Sim and DiScipio (1982), or by monoclonal antibody affinity chromatography (Moffatt & Sim, 1990). During storage of plasma and in isolation procedures, factor H (monomer M_r 150 000) undergoes a single proteolytic cleavage to form a structure consisting of the N-terminal approximately 38 000 M_r polypeptide disulfide linked to the approximately 120 000 M_r C-terminal polypeptide (Alsenz et al., 1985). This cleavage is probably mediated by plasmin (Bitter-Suerman et al., 1981). The factor H used in scattering studies contained less than 3% of this degraded form. The single cleavage of factor H can be mimicked by trypsin. A sample of factor H (20 mL, 950 μg/mL in 20 mM Tris-HCl, 150 mM NaCl, and 0.5 mM EDTA, pH 7.4) was digested with trypsin (2% w/w; Worthington, TPCK treated) for 15 min at 37 °C. The reaction was stopped by adding a 2-fold molar excess of soybean trypsin inhibitor (type I-S, Sigma) over trypsin. The products of digestion were analysed by SDS–PAGE and were shown to consist of 1–2% undigested factor H, 95% factor H cleaved into the required two-chain form, and 3–4% factor H that was more extensively degraded. This mixture was used to study the scattering properties of the two-chain form of factor H.

Sample Preparation for Solution Scattering. Protein samples (factor H or trypsin-cleaved factor H, 15–40 mg) were dialyzed against 20 mM potassium phosphate and 0.5 mM EDTA, pH 7.0, bound onto a column of DEAE-Sephacel (6 cm × 1.5 cm diameter) in the same buffer, and eluted as a single, high-concentration peak by washing in the same buffer containing 350 mM NaCl. Samples were then gel-filtered on a column (25 cm × 1.5 cm diameter) containing Sephacryl S-300 and Ultrogel AcA 34 (a 1:1 v/v mixture) in 12.4 mM sodium phosphate, 200 mM NaCl, and 0.5 mM EDTA, pH 7.0. This procedure removed aggregates and also the trypsin and soybean trypsin inhibitor from trypsin-cleaved factor H. A final concentration step was done with B15 Minicon concentrators (Amicon). Use of Minicon concentrators did not cause aggregation of factor H up to a concentration of about 7 mg/mL. In the gel filtration step, no aggregates of factor H were detected in initial work, and this step was omitted for most of the factor H samples used. Higher concentrations of factor H were obtained by precipitating factor H with 14% w/v poly(ethylene glycol) (PEG 3500, Sigma) and redissolving the pellet to the required volume. This procedure also did not cause aggregation of factor H, as assessed by analytical gel filtration.

To test the potential effects of ionic strength on oligomer formation in factor H, samples at the same concentration (4.5–5.4 mg/mL) were dialyzed into 12.4 mM sodium phosphate and 0.5 mM EDTA, pH 7.0, containing NaCl concentrations ranging from 20 to 1030 mM.

To test the potential effects of pH, samples were also dialyzed into 12 mM potassium phosphate, 140 mM NaCl, and 0.5 mM EDTA, at pH values of 5.0, 5.2, 6.0, 7.0, and 8.0, and also with 200 mM NaCl and 0.5 mM EDTA, pH 7.0. Further non-phosphate buffers at various pH values were used to eliminate possible effects of specific buffer salts. These included 10 mM Bis-Tris-HCl [[bis(2-hydroxyethyl)amino]-tris(hydroxymethyl)methane hydrochloride], 140 mM NaCl, and 0.5 mM EDTA, pH 5.8; 10 mM MES [2-(*N*-morpholino)ethanesulfonic acid], 150 mM NaCl, and 0.5 mM EDTA, adjusted to pH 7.2, 7.3, and 8.8 with Tris base; and 25 mM HEPPS [*N*-(2-hydroxyethyl)piperazine-*N*′-3-propanesulfonic acid], 140 mM NaCl, and 0.5 mM EDTA, at pH 7.8 and 8.9.

To test the effects of Zn^{2+} ions on factor H, samples were equilibrated in 10 mM PIPES [piperazine-*N*,*N*′-bis(2-ethanesulfonic acid)] and 140 mM NaCl, pH 7.0, to which aliquots of 0.1 M $ZnCl_2$ in this buffer were added to attain the required Zn^{2+} concentrations (Table I). Other factor H samples were dialyzed into 0.5 mM $ZnCl_2$, 25 mM PIPES, and 140 mM NaCl (pH 6.8–6.9). Other divalent metal chlorides, including $CoCl_2$, $HgCl_2$, $MgCl_2$, $MnCl_2$, and $NiCl_2$, were used as controls for the effect of Zn^{2+}. These were added at a final concentration of 100 μM to solutions of 10 mM PIPES and 140 mM NaCl, pH 7.0 (cf. Table I).

For calculation of relative M_r values by X-ray scattering, bovine chymotrypsinogen and trypsinogen (Sigma) and human complement component C3 were used as standards. Chymotrypsinogen and trypsinogen were treated repetitively with 2 mM diisopropyl fluorophosphate to stabilize the proteins and were purified by ion-exchange chromatography on a FPLC Mono S column (Pharmacia), equilibrated in 10 mM KH_2PO_4 (pH unadjusted), and eluted on a linear salt gradient up to 1 M KCl in the starting buffer. Hemolytically active C3 was purified as in Sim et al. (1981). Cleavage of the internal thiol

ester of C3 to give C3u was performed by incubating C3 with 100 mM methylamine at pH 9 for 1 h at 37 °C and subsequently dialyzing out the methylamine at 4 °C.

Factor H samples were analyzed by SDS–PAGE (Laemmli, 1970) before and after scattering experiments. Samples were prepared with and without reduction, for electrophoresis, as described by Fairbanks et al. (1971). No degradation of factor H after exposure to either X-ray or neutron beams was observed. A few factor H samples were assayed for cofactor activity (Sim & Sim, 1983) before and after scattering experiments. No significant alteration in activity was found. Sample concentrations c in the text were derived from their absorptions at 280 nm for use in M_r calculations (below) by using an A_{280} of 14.2 (Sim & DiScipio, 1982). Whaley et al. (1978) report a comparable value of 13.1 (not used). The prediction from the primary sequence gave a value of 16.7 (Perkins, 1986); this assumes six biantennary complex type oligosaccharides with 66 carbohydrate residues (Ripoche et al., 1988). The A_{280} values were also calculated from sequences for chymotrypsinogen (21.2), trypsinogen (16.6), and C3 and C3u (9.9).

X-ray and Neutron Solution Scattering Experiments. Synchrotron X-ray scattering experiments were performed in five sessions on the solution camera at station 7.3 (Nave et al., 1985) for the data of Figure 2, and in three sessions on that at station 8.2 (Towns-Andrews et al., 1989) at the SRS Daresbury, U.K. On average, the incident photon flux is approximately 10 times higher on station 8.2 compared to that on station 7.3. The operating energy of the synchrotron storage ring was 1.8 or 2.0 GeV. At 1.8 GeV, beam currents ranged from 75 to 325 mA, with sample–detector distances (SD) between 2.180 and 2.210 m and wavelength λ between 0.1604 and 0.1608 nm on station 7.3. At 2.0 GeV, beam currents varied between 50 and 275 mA, and experiments were performed with SD values of 2.69 and 3.345 m (λ = 0.1608 and 0.1509 nm) on station 7.3 and of 2.76–2.83 and 4.16 m (λ = 0.155 nm) on station 8.2. The Q range [$4\pi \sin\theta/\lambda$; 2θ = scattering angle] on the linear detector used for all measurements was calibrated using wet, slightly stretched rat tail collagen (diffraction spacing of 67 nm) and, occasionally, the dry adductor muscle of the North American clam *Mercenaria mercenaria* (spacing 14.4 nm) as standards. At station 7.3, the effective Q range was 0.06–1.05 nm^{-1} (four sessions) and 0.05–1.33 nm^{-1} (one session), and at station 8.2, this was 0.08–1.22 nm^{-1} (two sessions) and 0.06–0.91 nm^{-1} (one session). Detector responses to normalize scattering intensities were measured by use of a uniform radioactive source based on ^{55}Fe. To minimize background subtraction errors, samples and buffers were measured in alternation for equal counting times in the same sample cell (mica windows of 10–15-μm thickness), normalizing the curves on the basis of an ionization chamber positioned behind the sample. Sample temperatures were usually 19–22 °C, and sometimes 6–14 or 27 °C. Data collection times were usually 6 or 10 min, and occasionally 3 or 20 min. Data reduction was based on the programs SWANAL (station 7.3) and OTOKO (station 8.2), in which the background curve was subtracted from the sample curve, and the result was normalized with the detector response (Nave et al., 1985; P. Bendall, J. Bordas, M. H. C. Koch, and G. R. Mant, EMBL Hamburg and SERC Daresbury Laboratory, unpublished software).

Neutron solution scattering experiments were performed on instruments D11 (Ibel, 1976) (two sessions) and D17 (two sessions) at the high-flux reactor at the ILL, Grenoble. Guinier R_G data (see below) were collected on D11 with λ of 1.001 nm (wavelength spread $\Delta\lambda/\lambda$ of 9%) and SD of 10.00 or 10.50 m, and data at larger Q were obtained with SD of 2.00 or 2.50 nm. The Q ranges were therefore 0.02–0.22 and 0.10–1.00 nm^{-1} in that order. Other data were collected on D17 with λ of 1.60 nm ($\Delta\lambda/\lambda$ of 10%) at an SD of 3.46 nm, giving a Q range of 0.05–0.42 nm^{-1}, or with a λ of 1.101 nm at an SD of 3.46 or 1.40 m and a main beam–detector axis angle of 0° or 19.93° at 1.40 m to give Q ranges of 0.07–0.58, 0.2–1.4, and 0.7–3.1 nm^{-1} in that order. Samples were dialyzed into 0%, 70%, 80%, and 100% ^2H_2O buffers (by volume) over a 36–48-h period with four buffer changes at 6 °C. Neutron data were collected at temperatures of 10 or 20–22 °C. Data reduction followed standard procedures (Ghosh, 1989) using the programs RNILS, SPOLLY, RGUIM, and RPLOT. All runs were corrected for electronic noise and ambient neutron backgrounds by using a cadmium run. Buffer backgrounds were subtracted from the sample runs, and the difference were normalized by using the incoherent scattering of water from which an empty cell background had been subtracted.

X-ray and Neutron Data Analyses. The radius of gyration R_G of the macromolecules and the forward scattered intensity at zero angle $I(0)$ are obtained from the scattering curves at low Q by the Guinier equation (Glatter & Kratky, 1982):

$$\ln I(Q) = \ln I(0) - R_G^2Q^2/3$$

R_G quantifies the degree of elongation of the structure in a given solute–solvent contrast. $I(0)/c$ (c = sample concentration in mg/mL) leads to the calculation of molecular weights, either as absolute values from neutron data by referencing this to the incoherent scattering of water or as relative values from X-ray data (Kratky, 1963; Jacrot & Zaccai, 1981). For an elongated, rodlike structure, the Guinier equation is valid when the product QR_G is less than 0.7, which sets the upper limit on Q. The lower limit on Q for a sufficiently accurate R_G determination is given by $QD_{max} \leq \pi$, where D_{max} is the largest macromolecular dimension (Pilz et al., 1979). Since factor H is too elongated to meet these conditions, the analyses yield approximate R_G and $I(0)$ values (Figure 1), denoted $R_{G\text{-app}}$ and $I(0)_{app}$. For rodlike structures, the radius of gyration of the cross section R_{XS} is obtained at larger Q from (Glatter & Kratky, 1982)

$$\ln [I(Q)Q] = (\ln [I(Q)Q])_{Q\to 0} - R_{XS}^2Q^2/2$$

where $[I(Q)Q]_{Q\to 0}$ is the cross-sectional intensity at zero angle. The length of the longest axis of the structure L can be determined from (Perkins et al., 1986)

$$L = \pi I(0)/[I(Q)Q]_{Q\to 0}$$

If the structure resembles an elliptical cylinder, then (Glatter & Kratky, 1982)

$$L^2 = 12(R_G^2 - R_{XS}^2)$$

If the structure is constructed of two or more distinct rodlike subunits, joined at an angle such that their axes are not parallel, the cross-sectional Guinier plots lead to two linear regions (subscripted 1 and 2, in order of increasing Q) from which the number of subunits n is given empirically (Perkins et al., 1986) either by

$$n = L_2/L_1$$

or by

$$n = [I(Q)_1Q]_{Q\to 0}/[I(Q)_2Q]_{Q\to 0}$$

Stuhrmann neutron analyses of the R_G^2 and R_{XS}^2 values as a function of the reciprocal solute–solvent contrast $\Delta\rho^{-1}$ yield information on the internal structure (Ibel & Stuhrmann, 1976). If the macromolecule can be approximated as cen-

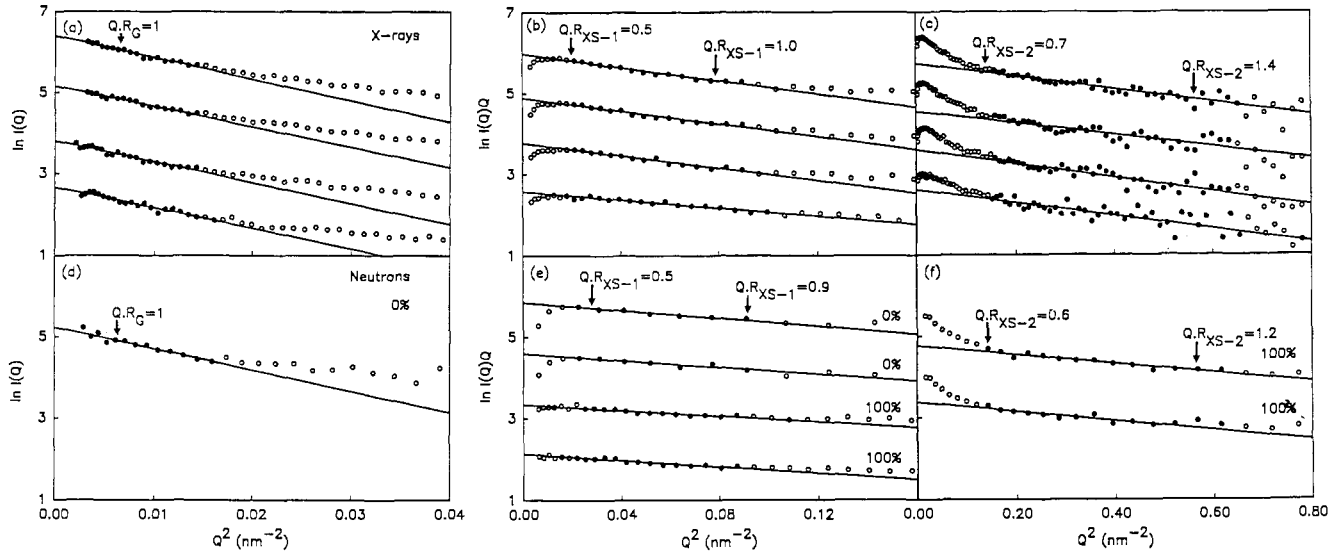

FIGURE 1: Guinier analyses of factor H by X-ray and neutron scattering. The curves are arbitrarily displaced on the intensity axis for clarity. Filled circles correspond to the $I(Q)$ data used to obtain $R_{G\text{-app}}$ or R_{XS} values, and the straight lines correspond to the best fit through these points. All scattering curves shown were measured in buffers of pH 6.8–7.3. (a) X-ray Guinier $R_{G\text{-app}}$ plots for factor H in MES and PIPES buffers at concentrations of 4.6 mg/mL (MES), 3.4 mg/mL (MES), 2.7 mg/mL (MES), and 2.0 mg/mL (PIPES), using a Q range of 0.06–0.12 nm^{-1} for fits. The QR_G values are based on an R_G of 12.4 nm. (b) X-ray $R_{XS\text{-}1}$ plots for factor H based on the scattering curves shown in (a), using a Q range of 0.15–0.30 nm^{-1} for fits. The $QR_{XS\text{-}1}$ values are based on an $R_{XS\text{-}1}$ of 3.6 nm. (c) X-ray $R_{XS\text{-}2}$ plots for factor H also using the curves shown in (a), using a Q range of 0.4–0.8 nm^{-1} for fits. The $QR_{XS\text{-}2}$ values are based on an $R_{XS\text{-}2}$ of 1.8 nm. (d) Neutron Guinier $R_{G\text{-app}}$ plot for factor H at 4.8 mg/mL in 0% ^2H_2O buffer, with the Q range as in (a) and QR_G calculated on the basis of an R_G of 12.6 nm. (e) Neutron $R_{XS\text{-}1}$ plots for factor H at 4.6 and 3.6 mg/mL in 0% ^2H_2O measured on instrument D11 at 2 m, and 4.4 and 2.4 mg/mL in 100% ^2H_2O measured on D17 at 3.46 m, using a Q range as in (b) for fits. The QR_{XS} values are based on an R_{XS} of 3.0 nm. (f) Neutron $R_{XS\text{-}2}$ plots for factor H at 0.8 and 1.2 mg/mL in 100% ^2H_2O using a Q range as in (c) for fits. The QR_{XS} values are based on an R_{XS} of 1.6 nm.

trosymmetric with respect to the distribution of internal scattering density fluctuations, which is true for glycoproteins (Perkins, 1988a,b), the Stuhrmann equation gives

$$R_G^2 = R_{G\text{-}C}^2 + \alpha_G \Delta\rho^{-1}$$

$$R_{XS}^2 = R_{XS\text{-}C}^2 + \alpha_{XS} \Delta\rho^{-1}$$

where $R_{G\text{-}C}$ and $R_{XS\text{-}C}$ are the radii of gyration at infinite contrast (when $\Delta\rho^{-1}$ is zero) and α_G and α_{XS} are the radial inhomogeneity of scattering density. Final analyses were carried out in London by using a common analysis and plotting program SCTPL (Perkins & Sim, 1986) for the Guinier analyses, and a weighted two-parameter least-squares method to analyze match-point and Stuhrmann plots.

Molecular Modeling Calculations. Scattering curve modeling was carried out by using overlapping Debye spheres to follow standard procedures (Glatter & Kratky, 1982) in application to synchrotron X-ray and neutron scattering data (Perkins & Weiss, 1983; Perkins, 1985; Perkins & Sim, 1986). The total unhydrated volume (187 nm^3) of factor H was calculated from the 1213 residues in the sequence (Ripoche et al., 1988) by using the crystallographic volumes for amino acids and carbohydrates (Chothia, 1975; Perkins, 1986). X-ray curve fitting (in a high positive solute-solvent contrast) is based on the hydrated volume. The total volume of the Debye sphere models was obtained from a hydration of 0.3 g of H_2O/g of glycoprotein and an electrostricted water molecule volume of 0.0245 nm^3 in place of the free water volume of 0.0299 nm^3 (Perkins, 1986). The final Debye models were generated by using spheres, with each sphere volume set to be that of the cube of side 1.27 nm. Neutron data correspond largely to the unhydrated glycoprotein volume, since the hydration shell that surrounds the macromolecule is invisible by the usual neutron contrast variation techniques (Perkins, 1986). This means that partial specific volumes $\bar{v}$ are larger if they are obtained from neutron match points instead of by densitometry. Neutron curve fitting was based on data in 0% and 100% ^2H_2O to correspond to high positive and negative solute–solvent contrasts, respectively, and the cube side was reset to 1.15 nm to correspond to the dry volume. The simulated neutron curves were corrected for wavelength spread and beam divergence (Cusack, 1981; Perkins & Weiss, 1983).

Modeling of the sedimentation coefficient $s^0_{20,w}$ was based on the hydrated volume as in the X-ray curve fitting, and this leads to a calculated partial specific volume $\bar{v}$ of 0.717 mL/g for factor H. When hydrodynamic spheres were used, this hydration is increased to 0.39 g in order to compensate for the void spaces between the nonoverlapping spheres (Perkins, 1989). Calculations were performed by using the program GENDIA (Garcia de la Torre & Bloomfield, 1977a,b).

Results and Discussion

Synchrotron X-ray Scattering Curves of Factor H at pH 7. X-ray solution scattering experiments were performed on native factor H at concentrations between 1.1 and 4.9 mg/mL at pH values of 6.8–7.3 in MES, PIPES, and phosphate buffers. Representative Guinier plots in Figure 1a in the Q range between 0.06 and 0.12 nm^{-1} appeared to be linear out to a QR_G of 1.0 and give an apparent radius of gyration R_G close to 12 nm. Since the center-to-center distance between adjacent SCR/CCPs has been estimated to range between 2.4 and 4.5 nm (Reid et al., 1986; Perkins et al., 1988; Bartow et al., 1989; Carrell et al., 1989; Moore et al., 1989), the total length of 20 SCR/CCPs in factor H would lie between 48 and 90 nm if the SCR/CCPs are fully extended in solution. The corresponding R_G would lie between 14 and 26 nm. The Guinier plots can underestimate the true R_G and $I(0)$ of factor H. These were therefore employed as an approximate measure of apparent R_G and $I(0)$ parameters for factor H, denoted as $R_{G\text{-app}}$ and $I(0)_{app}$, and were obtained from the same range of Q in all scattering curves.

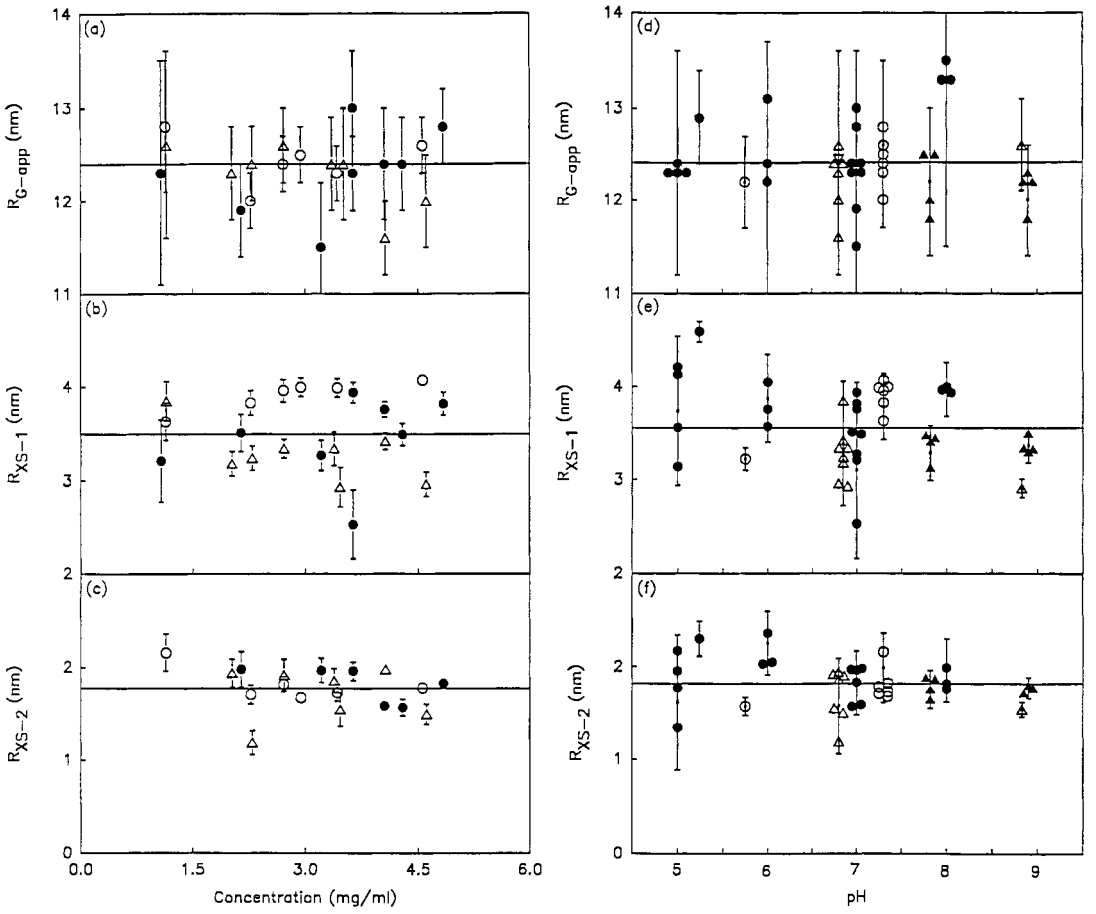

FIGURE 2: Concentration and pH dependence of the $R_{G\text{-}app}$, $R_{XS\text{-}1}$, and $R_{XS\text{-}2}$ data for factor H. The straight line corresponds to the mean of the data point shown. (a, b, and c) Concentration dependence between 1.1 and 4.9 mg/mL of the $R_{G\text{-}app}$, $R_{XS\text{-}1}$, and $R_{XS\text{-}2}$ data, respectively, at pH 6.8–7.3. Individual data points and their associated statistical errrors are shown. Data were obtained in four buffers containing 12 mM phosphate (●), 10 mM MES–Tris (○), and 25 mM PIPES (△), each with 140 or 150 mM NaCl and 0.5 mM EDTA (Materials and Methods). (d, e, and f) pH dependence of the $R_{G\text{-}app}$, $R_{XS\text{-}1}$, and $R_{XS\text{-}2}$ data, respectively. Data measured at each pH experiment were grouped together for clarity; errors represent the full range of statistical error found in the measurements. The samples were in 12 mM phosphate (●), 25 mM MES–Tris or Bis-Tris (○), 25 mM HEPPS (▲), and 10 mM Pipes (△), each with 140–150 mM NaCl and 0.5 EDTA in a pH range of pH 5.0–8.9 (Materials and Methods). The combined mean values are as follows: $R_{G\text{-}app}$, 12.4 ± 0.4 nm (43 values); $R_{XS\text{-}1}$, 3.6 ± 0.4 nm (43 values); $R_{XS\text{-}2}$, 1.8 ± 0.3 nm (41 values).

While small buffer subtraction errors affected a number of scattering curves close to the beam stop (and hence the $R_{G\text{-}app}$ determinations), 22 satisfactory X-ray spectra [defined as in Perkins et al. (1990a)] were collected in this pH range between 6.8 and 7.3. No concentration dependence was observed, and the mean X-ray $R_{G\text{-}app}$ of factor H was determined to be 12.3 ± 0.4 nm in this Q range (Figure 2a).

No limitation in the available Q range applies to the cross-sectional Guinier analyses (Pilz, 1982). The use of two Q ranges between 0.15 and 0.30 and between 0.4 and 0.8 nm^{-1} resulted in linear plots which yield two cross-sectional radii of gyration $R_{XS\text{-}1}$ and $R_{XS\text{-}2}$ (Figure 1b,c). No concentration dependence of $R_{XS\text{-}1}$ was observed in Figure 2b, and a mean value of 3.5 ± 0.5 nm was determined. The analysis of Figure 2c gave a mean $R_{XS\text{-}2}$ of 1.7 ± 0.4 nm.

X-ray Studies of Factor H as a Function of pH, Ionic Strength, and Peptide Cleavage. In order to span the pH range from pH 5 to pH 9, 21 additional X-ray spectra were obtained in concentrations between 0.6 and 5.1 mg/mL. In the three sessions where enough X-ray data were available, the relative values of $I(0)_{app}/c$ exhibited no concentration dependence, and this shows that the molecular weight of factor H is unchanged. Excluding the pH 7 data (Figure 2d–f), $R_{G\text{-}app}$ was found to be 12.5 ± 0.5 nm, $R_{XS\text{-}1}$ was 3.6 ± 0.4 nm, and $R_{XS\text{-}2}$ was 1.9 ± 0.3 nm. Comparison with the pH 7 data above showed no pH dependence. The mean X-ray data for factor H are thus summarized in the caption to Figure 2 for all 43 scattering curves.

To evaluate the effect of ionic strength on factor H, samples in pH 7.0 buffers (with 12 mM phosphate and 0.5 mM EDTA) were studied in the presence of 20, 50, 480, or 1030 mM NaCl at concentrations of 4.5–5.4 mg/mL. Analyses gave a mean $R_{G\text{-}app}$ of 12.9 ± 0.5 nm, an $R_{XS\text{-}1}$ of 4.0 ± 0.9 nm, and an $R_{XS\text{-}2}$ of 1.7 ± 0.2 nm, all of which are within error of the pH dependence study (Figure 2). To investigate the effect of polypeptide cleavage within the sixth SCR/CCP (SCR/CCP-6) of factor H between Arg313 and Arg314 (Ripoche et al., 1988), 14 scattering curves for split factor H (Materials and Methods) were measured in phosphate, MES, and PIPES buffers between pH 6.8 and 7.3. Analyses gave mean $R_{G\text{-}app}$, $R_{XS\text{-}1}$, and $R_{XS\text{-}2}$ values of 12.0 ± 1.2, 3.5 ± 0.6, and 1.9 ± 0.4 nm in that order. These are also within error of the values for native factor H (Figure 2). The relative $I(0)_{app}/c$ data showed that the molecular weight remained unchanged after cleavage. In conclusion, the overall solution structure of the 20 SCR/CCP domains in factor H is not affected by changes of concentrations between 1 and 5 mg/mL, pH values between 5 and 9, ionic strengths between 20 and 1030 mM NaCl, or polypeptide cleavage in SCR/CCP-6.

Radiation-Induced Structural Change in Factor H. The individual $R_{XS\text{-}1}$ data in Figure 2b show a spread of values that exceeds the magnitudes of the statistical errors. To investigate

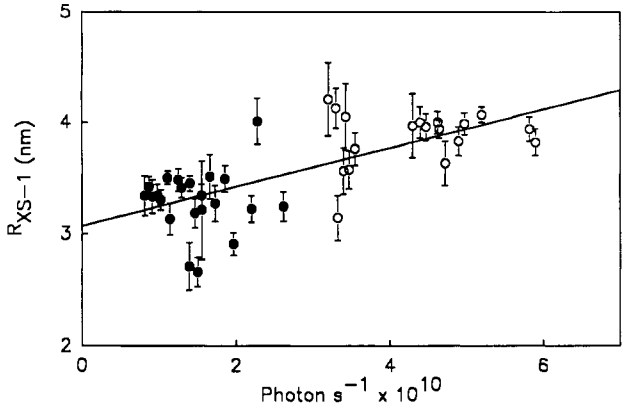

FIGURE 3: Dependence of the X-ray R_{XS-1} values of factor H on the incident flux of synchrotron radiation on the sample. Two storage ring energies of 1.8 GeV (●) and 2.0 GeV (○) at station 7.3 were used, for which the incident flux is 2.2×10^{10} and 5×10^{10} photons s^{-1}, respectively, for a beam current of 200 mA. The R_{XS-1} data are those of Figure 2e, and the beam current is that noted at the start of each sample data run. The Student's *t* test by MINITAB statistical analyses shows that the probability of the correlation of R_{XS-1} with the incident flux is significantly better than 99%. The intercept extrapolated to 0 photons s^{-1} gives an R_{XS-1} of 3.1 ± 0.1 nm (40 values). The corresponding analysis for R_{G-app} gives 12.0 ± 0.1 nm (41 values), and that for R_{XS-2} gives 1.7 ± 0.1 nm (37 values).

this, the R_{XS-1} data obtained on the camera at station 7.3 with two synchrotron ring energies were plotted against the X-ray flux incident on the sample. Figure 3 shows that a statistically valid dependence on the flux to better than 99% probability was observed. Analyses of the R_{G-app} and R_{XS-2} data do not show statistically significant trends (Figure 2 vs Figure 3). This observation was further tested in final sessions by the use of time-resolved spectroscopy at station 8.2, where the X-ray photon flux is approximately 10-fold greater. The R_{XS-1} values measured from the mean of the first five of the ten time frames recorded in 10 min were uniformly reduced when compared with that measured from all ten time frames, as expected, while the R_{G-app} and R_{XS-2} data were not affected. Occasionally, both the R_{G-app} and $I(0)_{app}$ values were observed to increase rapidly after 3–4 min during data collection on station 8.2. In this case, data analyses were based on the first three time frames. It is concluded that X-ray-induced structural changes have occurred in the domain structure of factor H. SDS gel electrophoresis on irradiated factor H samples do not show any change when compared to the preirradiated samples. The radiation-independent value of R_{XS-1} from MINITAB regression is 3.1 ± 0.1 nm (Figure 3) instead of the 3.6 ± 0.4 nm value previously determined (Figure 2e).

The M_r of factor H was determined from $I(0)/c$ by solution scattering by reference to M_r standards also measured during the same beam session after dialysis into the same buffer (10 mM PIPES, 140 mM NaCl, pH 7.1). In all, $I(0)/c$ data from 7 curves for chymotrypsinogen (1.9–7.4 mg/mL; M_r 25 600), 6 curves for trypsinogen (4.4–8.9 mg/mL; M_r 23 900), 13 curves for C3 (0.7–2.7 mg/mL; M_r 187 100), and 4 curves for C3u (0.9 mg/mL) were compared with the $I(0)_{app}/c$ values from 13 curves for factor H (3.8–7.5 mg/mL) measured within 3 min. All curves were checked for the absence of time-dependent effects. The M_r of factor H was determined as 254 000 or 299 000 (±33 000) if the absorption coefficient A_{280} is 16.7 or 14.2, respectively (Materials and Methods). Since $I(0)_{app}$ is reduced compared to $I(0)$ if this is measured just beyond the true Guinier region for a rodlike macromolecule, this calculation sets a lower limit to the value of M_r. Comparison with the M_r of 150 000 from the sequence and carbohydrate composition (Ripoche et al., 1988; Materials and Methods) shows clearly within systematic error that factor H is dimeric. Sim and DiScipio (1982) reported that factor H is monomeric from hydrodynamic data. Reasons for this discrepancy are possibly the higher concentrations of factor H used for the scattering experiments, or potential difficulties in the hydrodynamic diffusion coefficient measurements by gel filtration for a highly elongated macromolecule. Experiments to investigate this discrepancy are currently in progress.

Neutron Contrast Variation of Factor H at pH 7. Neutron scattering was carried out with factor H in order to extend the X-ray results. Factor H was studied in the same Q range in a concentration range of 0.6–4.9 mg/mL in buffers of pH 7.0 or 7.3. Absolute M_r calculations based on $I(0)_{app}/c$ data measured in H_2O (where systematic errors are minimized; Jacrot & Zaccai, 1981) gave 270 000 and 320 000 (±20 000) if A_{280} is 16.7 and 14.2, respectively. This confirms independently the X-ray result that factor H is dimeric. As a further control of the neutron data, analyses of the available $I(0)/c$, $[I(Q)_1Q]_{Q\to 0}/c$ and $[I(Q)_2Q]_{Q\to 0}/c$ data as a function of the contrast (12–13 points in each case: Figure 4a) gives match points of 38.8%, 40.2%, and 43.5% (±1%) ^2H_2O for factor H in that order. These are comparable to a predicted match point of 42.7% ^2H_2O calculated from the dry volume of factor H (Perkins, 1986).

The Stuhrmann plots of R_{G-app}^2, R_{XS-1}^2, and R_{XS-2}^2 as a function of the reciprocal solute–solvent contrast difference $\Delta\rho^{-1}$ will report on both the external and internal structure of factor H. The scattering properties of glycoproteins can be influenced by large scattering density inhomogeneities (Perkins et al., 1990b; Smith et al., 1990). The R_{G-app} analysis (Figure 4b) gives an $R_{G-app-C}$ of 12.6 ± 0.3 nm, and no contrast dependence was observed within error, as also found for other highly elongated complement components such as C1q (Perkins et al., 1984). This confirms the X-ray R_{G-app} value of 12.4 nm. Both the R_{XS-1} and R_{XS-2} data exhibit contrast-dependent behavior. At infinite solute–solvent contrast, the two R_{XS} values of 3.0 and 1.8 nm (Figure 4) agree with the X-ray determinations of R_{XS-1} of 3.1 nm (Figure 3) and R_{XS-2} of 1.8 nm in positive contrasts. Since radiation effects are not present in neutron scattering, Figure 4c confirms the analysis of R_{XS-1} in Figure 3. The positive slopes of the Stuhrmann plots (Figure 4c) indicate that the regions of higher scattering density (carbohydrate and hydrophilic amino acids; Perkins, 1986) are located nearer the surface of the cross section of factor H than the regions of lower scattering density. The slopes α_{XS-1} and α_{XS-2} are 43×10^{-5} and 15×10^{-5}. By use of published α data for protein and glycoproteins, α_{XS} is predicted to be $(17–65) \times 10^{-5}$ if R_{XS-1} is 3.0 nm and $(5–24) \times 10^{-5}$ if R_{XS-2} is 1.8 nm. Both the observed α_{XS} values lie within these ranges. Factor H therefore exibits a moderate degree of cross-sectional density inhomogeneity which is typical of proteins and glycoproteins.

Domain Structure of Factor H. The elongation ratio R_{G-app}/R_0 for factor H (where R_0 is the R_G of the sphere having the same volume as factor H) is based on the X-ray R_{G-app} (Figure 2) and the volume calculated from the sequence on the basis of a dimer (Chothia, 1975; Perkins, 1986) and is at least 3.6. Factor H is thus much more elongated than typical globular proteins where R_G/R_0 is 1.28 (Perkins, 1988a). Since many other plasma proteins of the immune system have large R_G/R_0 ratios usually between 1.7 and 3.2 (Perkins, 1989), factor H has one of the most elongated structures known for plasma proteins.

That two cross-sectional R_{XS} values were identified from the scattering analyses suggests that the domain structure of

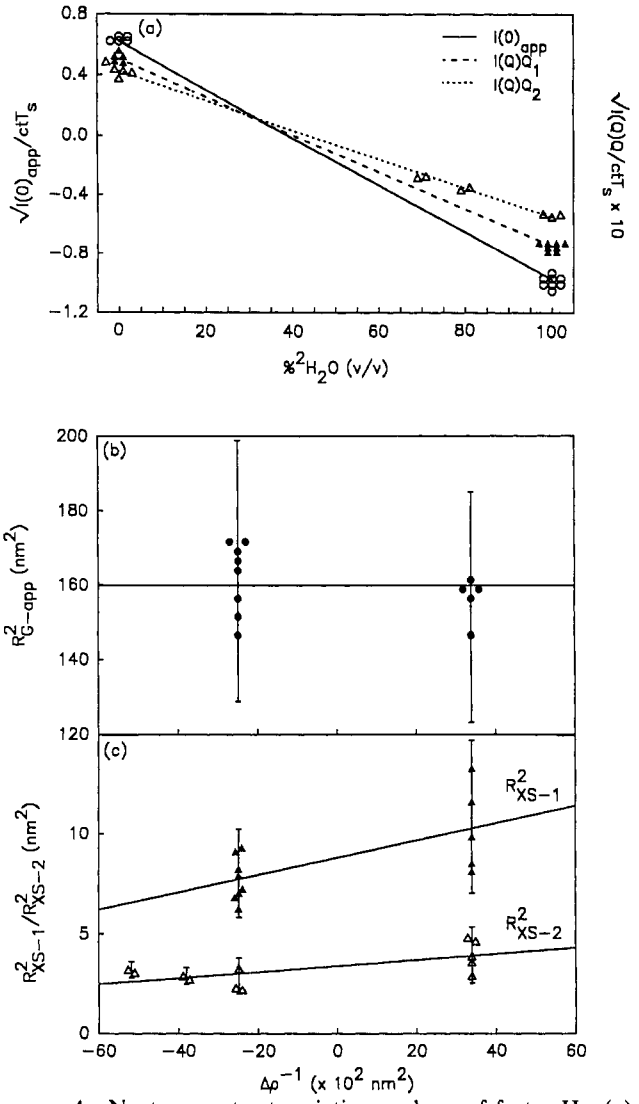

FIGURE 4: Neutron contrast variation analyses of factor H. (a) Match-point determinations. The values of $[I(0)_{app}/cT_s]^{1/2}$ (○) (c, concentration; t, sample thickness; T_s, transmission) are plotted against the volume percentage of ^2H_2O. The corresponding data for $[I(Q)_1Q]^{1/2}$ and $[I(Q)_2Q]^{1/2}$ are denoted by ▲ and △ in that order. (b) Stuhrmann plot of the $R_{G\text{-}app}{}^2$ data plotted against the reciprocal solute–solvent contrast difference $\Delta\rho^{-1}$. The line indicates the mean $R_G{}^2$ value, which corresponds to a $R_{G\text{-}app\text{-}C}$ of 12.6 ± 0.3 nm (13 values) and an $\alpha_{G\text{-}app}$ that is not measurable. (c) Corresponding Stuhrmann plots of the $R_{XS\text{-}1}{}^2$ (▲) and $R_{XS\text{-}2}{}^2$ (△) data. The MINITAB best-fit lines are shown in (a) and (c) and give the following Stuhrmann analysis: $R_{XS\text{-}C\text{-}1}$ = 3.0 ± 0.1 nm and $\alpha_{XS\text{-}1}$ = (43 ± 15) × 10^{-5} (13 values); $R_{XS\text{-}C\text{-}2}$ = 1.8 ± 0.1 nm and $\alpha_{XS\text{-}2}$ = (15 ± 5) × 10^{-5} (12 points). Data in 0% ^2H_2O were recorded by using 12 mM phosphate, pH 7.0, containing either 140 mM NaCl and 0.5 mM EDTA or 200 mM NaCl, or by using 10 mM MES–Tris, 150 mM NaCl, and 0.5 mM EDTA, pH 7.3. Data in 70%, 80%, and 100% ^2H_2O were recorded by using 12 mM phosphate and 200 mM NaCl, pH 7.0.

factor H is organized on two levels. The $R_{XS\text{-}2}$ of 1.8 ± 0.3 nm is within error of the best X-ray $R_{XS\text{-}2}$ determination of 2.1 ± 0.2 nm for C4BP at 1.45 mg/mL (Perkins et al., 1986). Since the sequences of both factor H and C4BP are largely composed of SCR/CCPs (91% in the case of C4BP), $R_{XS\text{-}2}$ can be assigned to the cross-sectional dimensions of a linear assembly of SCR/CCP domains. This is consistent with the lack of radiation-induced structural change in this region of the scattering curve.

The ratio of the cross-sectional intensities $[I(Q)_1Q]_{Q\to0}/[I(Q)_2Q]_{Q\to0}$ will give the number of subunits in factor H (Materials and Methods). The mean of 43 and 39 calculations for the two cross-sectional regions gives a ratio of 1.8 ± 0.4. This is interpreted to show that there are two distinct subunits in factor H. The $R_{XS\text{-}1}$ parameter is thus identified as a measure of the cross-sectional properties of the relative orientation of these two subunits, i.e., the two monomers of dimeric factor H.

Formation of Higher Oligomers in the Presence of Zn^{2+}. Zn^{2+} is one of the few known inhibitors of C3b cleavage by factor I and factor H (Crossley & Porter, 1980; Day & Sim, 1986). The binding of factor H, but not factor I or C3b, to a Zn^{2+}-chelate resin suggests that Zn^{2+} has a direct effect on factor H (Day & Sim, 1986). Synchrotron X-ray experiments were used to monitor the effect of additions of Zn^{2+} to factor H. In linear Guinier plots, large increases in both the $R_{G\text{-}app}$ and $I(0)_{app}/c$ parameters were observed, based on the Q range specified in Table I.

The X-ray measurements in Table I were performed after 10–500 μM Zn^{2+} had been added 9–15 h previously to factor H at 10.8 mg/mL. At 500 μM Zn^{2+}, precipitation occurred within 4 h. No concentration dependences of these Guinier parameters were observed except for the case of 200 μM Zn^{2+} where both $I(0)_{app}/c$ and $R_{G\text{-}app}$ increased on dilution. Relative M_r calculations based on the $I(0)_{app}/c$ data for native factor H as standard suggest that these oligomers continued on average between 3 and 11 monomers of factor H; this figure increases in proportion to the amount of Zn^{2+} present. Independent calculations of the total of subunits from the ratio of the $[I(Q)_1Q]_{Q\to0}$ and $[I(Q)_2Q]_{Q\to0}$ values in each curve (Materials and Methods) also showed that there were on average between 3 and 13 monomers per oligomer. Experiments in which factor H (1–5 mg/mL) was dialyzed against 500 μM Zn^{2+} prior to the X-ray experiments yielded oligomers with 8–10 subunits. Other experiments showed that the addition of 10–20 μM Zn^{2+} to factor H at 3.8 mg/mL caused the formation of similar oligomers within 3–12 min. The occurrence of higher oligomers of factor H in the presence of Zn^{2+} has also been confirmed by ultracentrifugation experiments (T. P. Clackson and R. B. Sim, unpublished results).

The $R_{G\text{-}app}$ analyses of the Zn^{2+} oligomers indicate that this lies between 15 nm (tetramers) and 17 nm (decamers) (Table I). These are larger than that of 12.4 nm for native factor H (Figure 2 and Table I). The $R_{XS\text{-}1}$ data were readily analyzed in linear Guinier fits in the slightly reduced Q range of 0.14–0.22 nm^{-1} compared to that used in Figure 1. The $R_{XS\text{-}1}$ values of 5.8 (tetramers) to 8.5 nm (decamers) are also larger than those of 3.1–4.7 nm observed for native factor H (Figure 2 and Table I). No radiation-induced variations in either the $R_{XS\text{-}1}$ or $[I(Q)_1Q]_{Q\to0}$ data were observed in the presence of Zn^{2+}. The increase in $R_{XS\text{-}1}$ suggests that oligomerization proceeds primarily by the side-by-side association of the long axis of the factor H dimers in the presence of Zn^{2+}, not by an end-to-end association. The mean $R_{XS\text{-}2}$ value is 1.8 ± 0.2 nm. Since this is within error of that measured for dimeric factor H (Figure 2 and Table I) and C4BP, this supports further the assignment of $R_{XS\text{-}2}$ as the cross-sectional parameter of a linear arrangement of SCR/CCP domains (see above).

Control X-ray scattering experiments based on the additions of 100 μM Co^{2+}, Hg^{2+}, Mg^{2+}, Mn^{2+}, and Ni^{2+} (which do not inhibit factor H) show that factor H remains dimeric under these conditions. This suggests that the specific inhibitory effect of Zn^{2+} is the result of its ability to cause factor H to rapidly form oligomers.

Table I: Effect of Zn^{2+} on Factor H[a]

Zn^{2+} concentration (μM)	$I(0)_{app}/c$	$I(Q)_1Q/c$	$I(Q)_2Q/c$	$R_{G\text{-app}}$ (nm)	$R_{XS\text{-}1}$ (nm)	$R_{XS\text{-}2}$ (nm)
0	4600 ± 400	28 ± 2[b]	10 ± 1	12.5 ± 0.3	4.7 ± 0.2[b]	1.7 ± 0.1
10	6300 ± 500	36 ± 3[c]	11 ± 2	14.9 ± 0.4	5.8 ± 0.3[c]	1.8 ± 0.2
20	6700 ± 300	41 ± 2	10 ± 1	14.6 ± 0.2	6.3 ± 0.1	1.9 ± 0.3
100	13900 ± 1200	81 ± 12	10 ± 1	15.7 ± 0.2	7.5 ± 0.2	1.9 ± 0.2
200	25000 ± 7200	121 ± 20	9 ± 1	17.3 ± 0.9	8.5 ± 0.3	1.7 ± 0.2

[a] In each row, samples were measured at factor H concentrations of 2.7, 5.5, 8.2, and 10.9 mg/mL. The mean values from Guinier analyses are reported. [b] In the absence of Zn^{2+}, these parameters are radiation-sensitive (Figure 3). The observed values are given. [c] In the presence of Zn^{2+}, the $I(Q)_1Q/c$ and $R_{XS\text{-}1}$ data were extracted by using a Q range of 0.14–0.22 nm^{-1}, not 0.15–0.30 nm^{-1} as for native factor H, while the Q ranges used for the $R_{G\text{-app}}$ and $R_{XS\text{-}2}$ values are as in Figure 1.

Hydrodynamic Simulations of Factor H. The sedimentation coefficient $s^0_{20,w}$ of factor H has been reported as 5.5–5.6 S (Whaley & Ruddy, 1976; Sim & DiScipio, 1982). This leads to a large calculated frictional ratio f/f_0 of 2.7 (assuming factor H to be dimeric), which is comparable to that of 2.1 for C4BP. This provides an independent measure of the degree of elongation of factor H. The modeling of $s^0_{20,w}$ data by the use of hydrodynamic sphere models is usually successful to ±0.2 S (Garcia de la Torre & Bloomfield, 1981; Perkins, 1989; Perkins & Nealis, 1989; Perkins et al., 1990b). Here, these calculations were used to assess the overall length of factor H.

Since solution scattering has shown that factor H is a dimer with a distinct two-subunit structure, factor H was represented by two rods joined at an angle (Figure 5). The increase of the join angle from 0° to 80° results in a sharp decline in the calculated $s^0_{20,w}$, which then remains steady on further angular increases up to 180°. For a given length of spheres, unique solutions are therefore obtained if the angle is less than 80°. If the dimer is represented by two lines of 20 hydrated nonoverlapping spheres of diameter 2.94 nm, each of length 59 nm, agreement with the experimental $s^0_{20,w}$, of 5.6 S is obtained if the join angle is 60°. If the dimer corresponds to two lines of 30 spheres of diameter 2.57 nm, each of length 77 nm, the join angle is 15°. If the dimer becomes two lines of 36 spheres of diameter 2.42 nm, each of length 87 nm, the join angle is 5°. In the latter case, if the error on $s^0_{20,w}$ is ±0.2 S, the error in the length is ±5 nm. The center-to-center separations of the 20 SCR/CCPs in factor H in that order are 2.9, 3.9, and 4.4 ± 0.3 nm.

Hydrodynamic calculations can likewise be made for three other SCR/CCP-containing proteins. The experimental s^0_{20w}, of 10.7–11.2 S for C4BP (seven subunits, each with 8 SCR/CCPs) and the X-ray scattering curves are in agreement with subunit lengths of 33 nm as observed by electron microscopy, and this corresponds to a SCR/CCP separation of 4.1 nm (Dahlbäck et al., 1983; Perkins et al., 1986) [Note: the effect of the small β-chain of C4BP which contains three SCR/CCPs in comparison to the 56 SCR/CCPs of the seven α-chains is negligible.] The b chain of factor XIII contains 10 SCR/CCPs and has a $s^0_{20,w}$ of 3.7 S (Ichinose et al., 1986; Carrell et al., 1989). This $s^0_{20,w}$ value corresponds to a hydrated rod (volume 129 nm^3) of length 30 nm or a line of 7 hydrated spheres of length 26 nm; both estimates are in agreement with electron microscopy, which reports a length of 30 nm (Carrell et al., 1989). This results in an SCR/CCP separation of 2.6–3.0 nm. Soluble recombinant CR2 (complement receptor type 2) contains 16 SCR/CCPs and has a $s^0_{20,w}$ of 4.5 S (Moore et al., 1987, 1989). Calculation shows that this is equivalent to a hydrated rod (volume 224 nm^3) of length 53 nm or a line of 19 hydrated spheres of length 55 nm; these lengths are however larger than the estimate of 39 ± 4 nm by electron microscopy (Moore et al., 1989). Here, the separation between the centers of the SCR/CCPs is either 3.3–3.4 or 2.4 nm in that order. A further estimate of 2.9 nm for the separation of the SCR/CCPs in CR1 (30 SCR/CCPs) has been reported, on the basis of a total length of 86 nm seen by electron microscopy (Bartow et al., 1989). These four length estimates between 2.4 and 4.1 nm correspond to the range of lengths allowed for factor H in the hydrodynamic simulations above. Smith et al. (1983) have however proposed that factor H has dimensions of 28 nm × 3 nm, and this implies that the SCR/CCPs are separated by 1.4 nm. This length is however incompatible with the hydrodynamic modeling and appears to be artifactually too low.

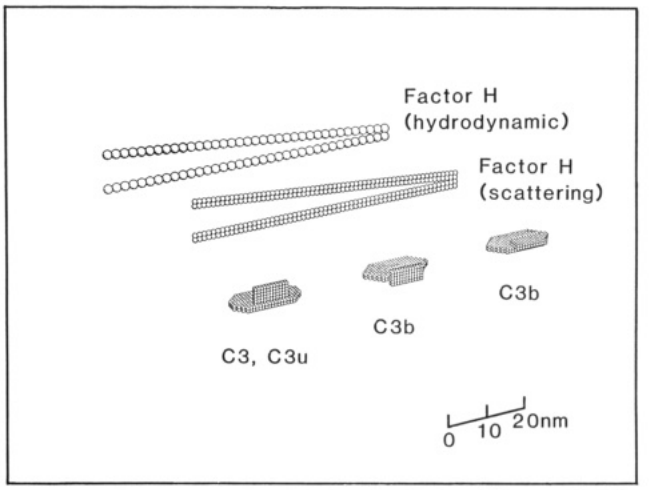

FIGURE 5: Comparison of models for C3, C3b, and factor H. The sphere models are a schematic representation of possible structures that are equivalent to the experimentally observed scattering curves and do not correspond to a unique structure determination. Beneath the models for factor H, a two-domain model for C3 and C3u and two for C3b are shown [following Perkins et al. (1990a)], with sphere diameters of 0.8 nm and overall length 18 nm. The relative orientation of the C3c and C3dg moieties alters on the activation of C3 to C3b; however, the accuracy of the models should not be overrated. These are compared with the two monomers of 61 × 2 × 1 spheres each (diameter 1.27 nm) set at a join angle of 5° used for the X-ray scattering curve model of factor H (Figure 6b) and the corresponding hydrodynamic model of 36 spheres per monomer (diameter 2.42 nm). The length of factor H is determined by the calculations of $s^0_{20,w}$; the angle between the two monomers is determined by the scattering curve simulations (Figure 6a).

Molecular Modeling of Factor H by Debye Simulations. In order to extend the modeling, X-ray and neutron scattering curves of factor H were fitted to Debye curves calculated from models on the basis of small overlapping spheres. These were based on two long rods joined at one end (Figure 5). In a series of simulations, the length of each rod was varied between 56 and 91 nm, the cross section of the rod was set as 2 × 1 spheres or 3 × 1 spheres, and the join angle was varied between 0° and 180°. The calculated curves were found to be insensitive to the total length in the Q range accessible to experiment; solution scattering is therefore not able to determine the length of factor H. The use of different rod cross sections had no

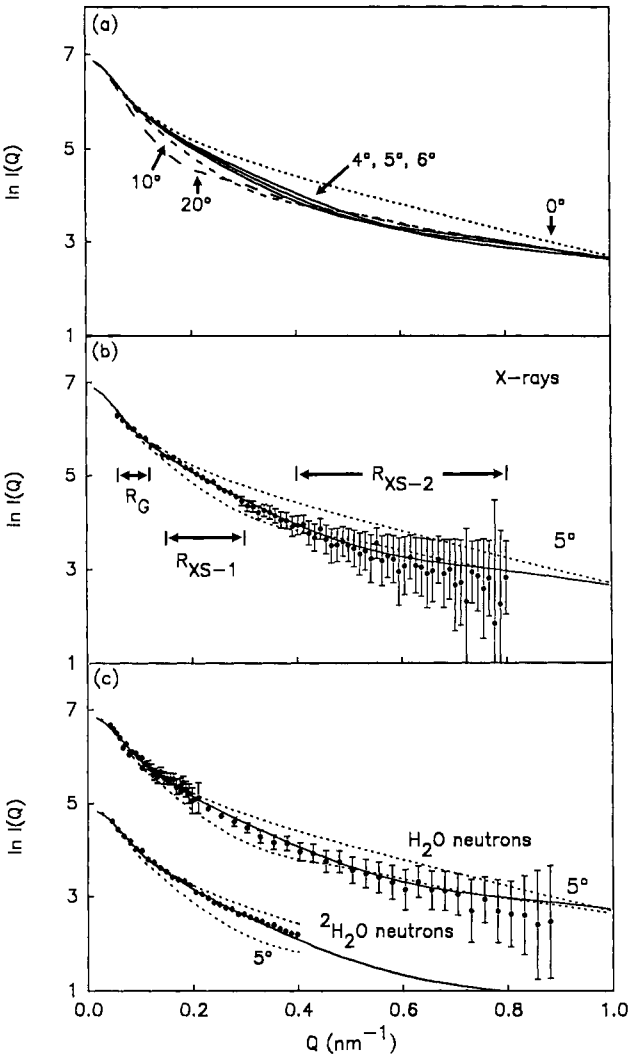

FIGURE 6: Molecular modeling of the scattering curves for factor H. The simulated curves (—) are based on the model shown in Figure 5 with an angle of 5° between the two linear rods. Experimental data are denoted by ●, and statistical errors are shown by error bars. (a) Theoretical curve simulations for join angles of 0° (···), 4°, 5° and 6° (—), and 10° and 20° (---), all as arrowed and based on the hydrated model used for (b). (b) The X-ray synchrotron curve at low incident flux is compared with the hydrated model with a join angle of 5°. The Q ranges used to measure $R_{G\text{-app}}$, $R_{XS\text{-}1}$, and $R_{XS\text{-}2}$ (Figure 1) are indicated. (c) Neutron scattering curves in 0% and 100% ^2H_2O are compared with the smeared curve from the unhydrated model (join angle of 5°). In (b) and (c), the theoretical curves for join angles of 0° and 10° (···) from (a) are shown also for comparison.

significant effect, and the final modeling employed that of 2 × 1 spheres. Figure 6a however showed that the calculated curves are sensitive to the join angle. Join angles of 0° or greater than 10° resulted in large deviations from the experimental data, and such models can therefore be eliminated. It is however emphasized that the solution scattering data can only be used to determine the best-fit join angle for the selected model. It is possible that other models may provide an equally good fit.

Analysis of several V-shaped hydrated models showed that the $R_{XS\text{-}1}$ and $R_{XS\text{-}2}$ regions of the experimental X-ray scattering curve could be readily fitted within statistical error (at low incident X-ray flux) in Figure 6b, by using a join angle of 5°. A clear difference between the simulated and experimental curves (not shown) was encountered with the X-ray data collected at high incident fluxes, as expected from Figure 3. The corresponding dry V-shaped models led to good fits of the neutron data in 0% and 100% H_2O in Figure 6c, again by using a join angle of 5°. The difference between negative and positive contrasts in the neutron data for factor H was not found to be significant, in accordance with the low Stuhrmann α values (Figure 4). The R factors (Smith et al., 1990) indicate the goodness of fit by analogy with crystallography, and typically these should be 0.020 or less. These were found to be 0.021, 0.016, and 0.007 in that order for the X-ray data and the 0% and 100% ^2H_2O neutron data in the Q range up to 0.8 nm^{-1}. Shorter rods were found to give slightly improved R values; longer rods led to poorer R values. By comparison, R was 0.036 for the fit using data collected at high X-ray flux.

In conclusion, these simulations show that there is a requirement for two subunits in factor H in order to obtain fits to the scattering curves and that the angle between these is close to 5°. The length of factor H cannot be determined by this method. The complementary hydrodynamic modeling indicates the overall length of factor H to be 87 ± 5 nm for a join angle of 5°. The final Debye model in Figure 5 was constructed from two rods of 61 × 2 × 1 spheres with a join angle of 5°. Each rod was set to be 77 nm in length in order to represent a reasonable SCR/CCP separation of 4 nm. The R_G values of the X-ray and neutron models are calculated to be 21–23 nm. As expected, these were experimentally unmeasurable, being almost double the value of $R_{G\text{-app}}$ observed in Figure 1. The R_G/R_0 ratio of the final model is 5.9.

Conclusions

Factor H is dimeric at concentrations between 1 and 11 mg/mL and pH values between 5 and 9. This is shown by the M_r determinations by both X-ray and neutron scattering. Dimerization implies that factor H has two binding sites for C3b and not one in the concentration range studied. The physiological concentration range of factor H in plasma is 0.2–0.6 mg/mL; satisfactory solution scattering data in this concentration range could not be obtained. Since C3b is deposited in clusters on surfaces (Sim et al., 1981), the factor H dimer may interact with two closely spaced C3b molecules on surfaces, thus increasing the apparent affinity for surface-bound C3b. Factor H is therefore more analogous in its oligomeric properties to the corresponding complement control protein of the classical pathway C4BP (which has up to seven C4b binding sites) than previously believed. Zinc is one of the few known inhibitors of factor H. The present experiments show that that this is strongly correlated with the Zn^{2+}-induced oligomerization of factor H dimers to form higher oligomers. Interestingly Zn^{2+} is reported to be an inhibitor of the factor I mediated release of CR1-bound immune complexes and degradation of cell-bound C3b and C4b (Jepsen et al., 1990); Day and Sim (1986) point out that Zn^{2+} also binds to CR1 and C4BP.

Evidence that the two monomers of native factor H are organized into a V-shape was obtained from the determination of the ratio of intensities $[I(Q)Q]_{Q\to 0}$ in the two cross-sectional plots to be close to 2 and the observation of two distinct R_{XS} values in the scattering curves. This was confirmed by the modeling calculations, in particular, when the curve simulation for factor H at join angles of 4°–6° in Figure 6a is compared with a join angle of 0°. Electron microscopy images also reveal such a V-shape, albeit in a more splayed-out form (Day, 1988). This splayed structure is analogous to that reported for C4BP in which the seven subunits are in a similar proximate arrangement (Dahlbäck et al., 1983; Perkins et al., 1986). No information on the assignment of a dimerization site to one or more SCR/CCPs in factor H is available at present from sequence data. It is not possible to infer whether the 20

SCR/CCPs lie parallel or antiparallel to each other in the dimer.

In joint solution scattering and hydrodynamic analyses to date, calculations of the overall macromolecular length leads to a estimated center-to-center separation of the SCR/CCPs of about 4 nm for factor H, C4BP, and the complement subcomponents C1r and C1s (Results and Discussion; Perkins et al., 1986; Perkins & Nealis, 1989). Comparison of these separations in solution with the length estimate of 4.2–4.6 nm for a single SCR/CCP (Perkins et al., 1988) suggests that the SCR/CCPs are joined end to end to form highly extended structures. This appears to be a general result. This separation is however reduced to 2.6–3.4 nm for the b chain of factor XIII and CR2, according to the hydrodynamic data of Moore et al. (1989) and Carrell et al. (1989). No explanation for this reduction is available at present; however, the unlikely possibility that the SCR/CCPs adopt a different conformation in these proteins cannot be ruled out at present.

Electron microscopy is performed in vacuo under nonphysiological conditions, with the use of stains and the possibility of beam damage and magnification errors. These factors may explain why the separations of the SCR/CCPs deduced from electron microscopy have ranged from 1.4 and 2.4 nm at one extreme to 4.1 nm at the other. This emphasizes the importance of studying macromolecular structures in solution. Generally, however, the use of electron microscopy leads to a similar conclusion for the extended arrangement of SCR/CCPs within C4BP, factor H, the b chain of factor XIII, CR1, and CR2 (Dahlbäck et al., 1983; Smith et al., 1983; Carrell et al., 1989; Bartow et al., 1989; Moore et al., 1989).

Figure 5 compares the size of C3 and C3b with the scattering and hydrodynamic models for factor H. The length of C3 and C3b is 18 nm (Perkins & Sim, 1986; Perkins et al., 1990a; Ikai et al., 1990), while that for factor H is close to 80 nm for each monomer. The N-terminal five SCR/CCPs in factor H are implicated in cofactor activity (Alsenz et al., 1985; Misasi et al., 1989). It is noteworthy that the 20-nm length of these five SCR/CCPs is slightly larger than the length of the longest axis of C3 and C3b; however, the number of SCR/CCPs in factor H that directly interact with C3b is not known at present. Studies with CR1 show that the N-terminal pairs of adjacent SCR/CCPs in each long homologous repeat of seven SCR/CCPs are responsible for the interactions with C3b or C4b; similar studies with CR2 show that the N-terminal pair of SCR/CCPs interact with C3dg (Klickstein et al., 1988; Nemerow et al., 1989; Lowell et al., 1989). It is likely that the role of the noninteracting SCR/CCPs in factor H, C4BP, CR1, and CR2 is to space apart the binding sites for C3b and C4b in order that these may bind to their control proteins. In addition to the C3b binding site and also a site for factor H dimerization, factor H has site(s) for binding to a receptor (Erdei & Sim, 1987) and for polyanion binding associated with its role in discriminating between alternative pathway activators and nonactivators (Meri & Pangburn, 1990). A large number of SCR/CCP domains with no specialized binding function may be required to space apart these different functional regions.

Acknowledgments

We thank Dr. W. Bras, Dr. C. Nave, Dr. E. Towns-Andrews and Dr. H. Gerritsen for instrumental support at the SRS Daresbury, Dr. A. J. Day, Dr. J. Torbet, and Dr. P. A. Timmins for experimental and instrumental support at the ILL Grenoble, and Miss B. E. Moffatt for expert technical assistance.

Registry No. Factor H, 80295-65-4; Zn, 7440-66-6.

References

Alsenz, J., Schulz, T. F., Lambris, J. D., Sim, R. B., & Dierich, M. P. (1985) *Biochem. J. 232*, 841–850.

Bartow, T., Klickstein, L., Wong, W., Roux, K., & Fearon, D. (1989) *FASEB J. 3*, 501 (Abstract).

Bitter-Suerman, D., Burger, R., & Hadding, U. (1981) *Eur. J. Immunol. 11*, 291–295.

Carrell, N. A., Erickson, H. P., & McDonagh, J. (1989) *J. Biol. Chem. 264*, 551–556.

Chothia, C. (1975) *Nature (London) 254*, 304–308.

Crossley, L. G., & Porter, R. R. (1980) *Biochem. J. 191*, 173–182.

Cusack, S. (1981) *J. Mol. Biol. 145*, 539–541.

Dahlbäck, B., Smith, C. A., & Müller-Eberhard, H. J. (1983) *Proc. Natl. Acad. Sci. U.S.A. 80*, 3461–3465.

Day, A. J. (1988) D. Phil. Thesis, University of Oxford.

Day, A. J., & Sim, R. B. (1986) *Biochem. Soc. Trans. 14*, 73–74.

Erdei, A., & Sim, R. B. (1987) *Biochem. J. 246*, 149–156.

Fairbanks, G., Steck, T. L., & Wallach, D. F. H. (1971) *Biochemistry 10*, 2606–2617.

Garcia de la Torre, J., & Bloomfield, V. A. (1977a) *Biopolymers 16*, 1747–1761.

Garcia de la Torre, J., & Bloomfield, V. A. (1977b) *Biopolymers 16*, 1779–1793.

Garcia de la Torre, J., & Bloomfield, V. A. (1981) *Q. Rev. Biophys. 14*, 87–139.

Ghosh, R. E. (1989) Internal Publication 89GH02T, Institut Laue Langevin, Grenoble, France.

Glatter, O., & Kratky, O., Eds. (1982) *Small-angle X-ray scattering*, Academic Press, New York.

Ibel, K. (1976) *J. Appl. Crystallogr. 9*, 269–309.

Ibel, K., & Stuhrmann, H. B. (1975) *J. Mol. Biol. 93*, 255–266.

Ichinose, A., McMullen, B. A., Fujikawa, K., & Davie, E. W. (1986) *Biochemistry 25*, 4633–4638.

Ikai, A., Nishigai, M., Saito, A., Sinohara, H., Muto, Y., & Arata Y. (1990) *FEBS Lett. 260*, 291–293.

Jacrot, B., & Zaccai, G. (1981) *Biopolymers 20*, 2413–2426.

Jepsen, H. H., Teisner, B., & Svehag, S.-E. (1990) *Scand. J. Immunol. 31*, 397–403.

Klickstein, L. B., Bartow, T. J., Miletic, V., Rabson, L. D., Smith, J. A., & Fearon, D. T. (1988) *J. Exp. Med. 168*, 1699–1717.

Kratky, O. (1963) *Prog. Biophys. Chem. 13*, 105–173.

Kristensen, T., & Tack, B. F. (1986) *Proc. Natl. Acad. Sci. U.S.A. 83*, 3963–3967.

Laemmli, U. K. (1970) *Nature 227*, 680–685.

Lowell, C. A., Klickstein, L. B., Carter, R. H., Mitchell, J. A., Fearon, D. T., & Ahearn, J. M. (1989) *J. Exp. Med. 170*, 1931–1946.

Meri, F., & Pangburn, M. K. (1990) *Proc. Natl. Acad. Sci. U.S.A. 87*, 3982–3986.

Misasi, R., Huemer, H. P., Schwaeble, W., Sölder, E., Larcher, C., & Dierich, M. P. (1989) *Eur. J. Immunol. 19*, 1765–1768.

Moffatt, B. E., & Sim, R. B. (1990) *Immunol. Lett.* (submitted for publication).

Moore, M. D., Cooper, N. R., Tack, B. F., & Nemerow, G. R. (1987) *Proc. Natl. Acad. Sci. U.S.A. 84*, 9194–9198.

Moore, M. D., DiScipio, R. G., Cooper, N. R., & Nemerow, G. R. (1989) *J. Biol. Chem. 264*, 20576–20582.

Nave, C., Helliwell, J. R., Moore, P. R., Thompson, A. W., Worgan, J. S., Greenall, R. J., Miller, A., Burley, S. K.,

Bradshaw, J., Pigram, W. J., Fuller, W., Siddons, D. P., Deutsch, M., & Tregear, R. T. (1985) *J. Appl. Crystallogr. 18*, 396–403.
Nemerow, G. R., Mullen, J. J., III, Dickson, P. W., & Cooper, N. R. (1989) *Complement Inflamm. 6*, 374 (Abstract).
Perkins, S. J. (1985) *Biochem. J. 228*, 13–26.
Perkins, S. J. (1986) *Eur. J. Biochem. 157*, 169–180.
Perkins, S. J. (1988a) *N Compr. Biochem. 18B*, Part II, 143–264.
Perkins, S. J. (1988b) *Biochem. J. 254*, 313–327.
Perkins, S. J. (1989) in *Dynamic Properties of Biomolecular Assemblies* (Harding, S. E., & Rowe, A. J., Eds.) pp 226–245, Royal Society of Chemistry, London.
Perkins, S. J., & Weiss, H. (1983) *J. Mol. Biol. 168*, 847–866.
Perkins, S. J., & Sim, R. B. (1986) *Eur. J. Biochem. 157*, 155–168.
Perkins, S. J., & Nealis, A. S. (1989) *Biochem. J. 263*, 463–469.
Perkins, S. J., Villiers, C. L., Arlaud, G. J., Boyd, J., Burton, D. R., Colomb, M. G., & Dwek, R. A. (1984) *J. Mol. Biol. 179*, 547–557.
Perkins, S. J., Chung, L. P., & Reid, K. B. M. (1986) *Biochem. J. 233*, 799–807.
Perkins, S. J., Haris, P. I., Sim, R. B., & Chapman, D. (1988) *Biochemistry 27*, 4004–4012.
Perkins, S. J., Nealis, A. S., & Sim, R. B. (1990a) *Biochemistry 29*, 1167–1175.
Perkins, S. J., Smith, K. F., Amatayakul, S., Ashford, D., Rademacher, T. W., Dwek, R. A., Lachmann, P. J., & Harrison, R. A. (1990b) *J. Mol. Biol. 214*, 751–763.
Pilz, I. (1982) in *Small Angle X-ray Scattering* (Glatter, O., & Kratky, O., Eds.) pp 239–293, Academic Press, London.
Pilz, I., Glatter, O., & Kratky, O. (1979) *Methods Enzymol. 61*, 148–249.
Reid, K. B. M., & Day, A. J. (1989) *Immunol. Today 10*, 177–180.
Reid, K. B. M., Bentley, D. R., Campbell, R. D., Chung, L. P., Sim, R. B., Kristensen, T., & Tack, B. F. (1986) *Immunol. Today 7*, 230–234.
Ripoche, J., Day, A. J., Harris, T. J. R., & Sim, R. B. (1988) *Biochem. J. 249*, 593–602.
Sim, E., & Sim, R. B. (1983) *Biochem. J. 210*, 567–576.
Sim, R. B., & DiScipio, R. G. (1982) *Biochem. J. 205*, 285–293.
Sim, R. B., & Perkins, S. J. (1989) *Curr. Top. Microbiol. Immunol. 153*, 209–222.
Sim, R. B., Twose, T. M., Paterson, D. S., & Sim, E. (1981) *Biochem. J. 193*, 115–128.
Sim, R. B., Malholtra, V., Day, A. J., & Erdei, A. (1987) *Immunol. Lett. 14*, 183–190.
Smith, C. A., Pangburn, M. K., Vogel, C.-W., & Müller-Eberhard, H. J. (1983) *Immunobiology 164*, 298 (Abstract).
Smith, K. F., Harrison, R. A., & Perkins, S. J. (1990) *Biochem. J. 267*, 203–212.
Towns-Andrews, E., Berry, A., Bordas, J., Mant, G. R., Murray, P. K., Roberts, K., Sumner, I., Worgan, J. S., Lewis, R., & Gabriel, A. (1989) *Rev. Sci. Instrum. 60*, 2346–2349.
Whaley, K., & Ruddy, S. (1976) *J. Exp. Med. 144*, 1147–1163.
Whaley, K., Widener, H., & Ruddy, S. (1978) in *Clinical Aspects of the Complement System* (Opferkuch, W., Rother, K., & Schultz, D. R., Eds.) pp 99–112, G. Thieme Verlag, Stuttgart.

Site-Dependent Inhibition by Single O^6-Methylguanine Bases of SV40 T-Antigen Interactions with the Viral Origin of Replication†

M. Bignami,*,‡ P. Karran, and D. P. Lane
Imperial Cancer Research Fund, Clare Hall Laboratories, South Mimms, Herts EN6 3LD, U.K.
Received October 17, 1990; Revised Manuscript Received December 10, 1990

ABSTRACT: The effects of O^6-methylguanine on the reactions involved in initiation of DNA replication were investigated by measuring the interactions of SV40 T antigen with oligonucleotides substituted with the methylated base. O^6-Methylguanine residues were positioned in either binding site I or binding site II of the SV40 origin of replication. Binding of purified T antigen, measured by both nitrocellulose filter binding and delayed oligonucleotide migration, was unaffected by the presence of seven methylated bases in binding site II. Single substitutions within binding site I were sufficient to inhibit T-antigen binding, and the extent of inhibition was dependent on the position of O^6-methylguanine in the DNA sequence. Unwinding by T antigen was analyzed by measuring displacement of a single-stranded oligonucleotide from similarly substituted, partially duplex substrates. The presence of three O^6-methylguanine residues in binding site I facilitated the helicase activity of T antigen. In contrast, single O^6-methylguanine bases inhibited unwinding. A correlation was observed between the position of the methylated base and the inhibition of both binding and unwinding by T antigen.

Although cells have evolved efficient strategies for the removal of damaged residues from DNA, occasional unrepaired lesions may escape surveillance and interact with cellular DNA replication. This interaction will occur more frequently in cells in which DNA repair enzymes are defective or absent. The specific DNA repair protein O^6-methylguanine (O^6-MeG)–DNA methyl transferase (MT) is not expressed in certain human cell lines [the Mex^- or Mer^- phenotype (Day et al., 1980; Sklar & Strauss, 1981)], resulting in a cellular sensitivity to alkylating agents that introduce O^6-MeG into DNA (Scudiero et al., 1984). Although the mechanism of cytotoxicity

† M.B. was supported in her stay at the Imperial Cancer Research Fund by a grant from the European Science Foundation.
* To whom correspondence should be addressed.
‡ Present address: Istituto Superiore di Sanita', Viale Regina Elena 299, 00161 Rome, Italy.

0006-2960/91/0430-2857$02.50/0